Aiming factor to flatten the flux distribution on cylindrical receivers

Alberto Sánchez-González[a,*], María Reyes Rodríguez-Sánchez[a], Domingo Santana[a]

[a]*Energy Systems Engineering Group (ISE), Department of Thermal and Fluid Engineering, Universidad Carlos III de Madrid, Av. Universidad, 30, 28911 Leganés, Madrid, Spain*

Abstract

High incident flux gradients and hot spots lead to extreme thermal stresses that may damage and reduce the lifetime of central receivers. An aiming strategy based on a single parameter, k, named aiming factor, is developed to generate symmetric flux maps about the receiver equator. By means of this k factor, ranging between 3 (generally equivalent to equatorial aiming) and 0 (alternatively aiming to top and bottom borders), the solar flux incident on the receiver and the spillage losses can be controlled. For each sector in a heliostat field, the aiming factor values causing the flattest symmetric flux maps, k_{flat}, are deterministically found with a sweep and mesh shifting procedure. Results for Dunhuang solar power tower plant show that k_{flat} is fairly constant throughout the year, except near sunrise and sunset in east and west sectors, respectively.

Keywords: Solar power tower, Heliostat spillage, Symmetric flux map, Flat concentration profile, FluxSPT tool

1 Nomenclature

AC	Cell area in the receiver mesh [m^2]
AFD	Allowable flux density [W/m^2]
AM	Mirror area of the heliostat [m^2]

---

*Corresponding author
Email address:* `asgonzal@ing.uc3m.es` (Alberto Sánchez-González)

BR_k	Beam radius based on k [m]
C	Concentration ratio of flux density [-]=[suns]
D	Receiver diameter [m]
DNI	Direct normal irradiation [W/m^2]
F	Flux density [W/m^2]
f	Loss factor [-]
H	Receiver height [m]
k	Aiming factor [-]
$\mathbf{n}$	Heliostat normal vector
$RMSD$	Root Mean Square Deviation
$\mathbf{s}$	Sun vector
SR	Slant range [m]
$\mathbf{t}$	Target vector
X, Y, Z	Cartesian coordinate axes

2   *Greek symbols*

ϵ	Elevation angle [rad]
η	Efficiency [-]
ω	Incidence angle [rad]
σ	Gaussian error [mrad]

3   *Subscripts*

e	Effective
h	Heliostat
i, j, p	Nodes in receiver mesh
max	Maximum
si	Image plane system of coordinates
slp	Slope
sp	Spillage
st	Target system of coordinates
sun	Sunshape
trk	Tracking

4   *Acronyms*

DAPS	Dynamic Aim Processing System
FluxSPT	Flux Solar Power Tower software tool
MCRT	Monte Carlo Ray Tracing
PID	Proportional Integral Derivative controller
PS10	Planta Solar 10 MW
PSA	Plataforma Solar de Almería
SAPS	Static Aim Processing System
SPT	Solar Power Tower
UNIZAR	Universidad de Zaragoza tool

1. Introduction

In Solar Power Tower (SPT) plants, direct radiation is concentrated by thousands of heliostats onto a tower-mounted central receiver, where a circulating working fluid is heated to eventually produce electricity [1]. Single equatorial aiming leads to the highest receiver interception, but also to unacceptable peak fluxes that have to be avoided or minimized. For successful operation of these plants, the heliostat field aiming strategy must protect the receiver from damage (thermal stress cracking, hot spots and corrosion), at the same time that the thermal output is maximized.

As long as SPT technology is being commercially deployed worldwide, the development of efficient aiming strategies is receiving great attention from the academic community in recent years. Metaheuristic methods, such as Tabu search and Genetic Algorithm, were applied to uniform the flux distribution in flat plate [2, 3] and cavity receivers [4, 5]. By means of an ant colony metaheuristic, the output of concentrated photovoltaic receivers [6] and molten salt receivers [7] was optimized. Astolfi et al. [8] proposed several optimization approaches to reduce the peak flux in a cylindrical receiver. A teaching-learning-based optimization was investigated to homogenize the flux on a flat receiver [9], and a closed-loop PID control was virtually implemented on Gemasolar plant [10]. Likewise, binary integer linear programming was virtually implemented on PS10 plant to homogenize the flux distribution on the flat plate receiver [11].

In Solar Two plant, two software systems controlled the field aiming: SAPS (static aim processing system) and DAPS (dynamic aim processing system). Using the first system, the target point of each heliostat was adjusted every 10 minutes because of sun movement, whereas heliostats caus-

ing overheating were removed from tracking with DAPS [12]. In PSA tower plant, named CESA-1, a knowledge-based heuristic selected the optimal aim points to control the air temperature in the volumetric receiver [13]; and, a distributed optimization algorithm was recently performed to uniform the flux distribution [14].

In order to procure symmetric flux maps, Vant-Hull suggested an aiming strategy where each row of heliostats is alternatively aimed to the top and to the bottom half of the receiver [15]. This strategy was further developed by the authors in Ref. [16], where it was succinctly introduced the concept of aiming factor.

The aiming factor approach [16], that has been utilized in recent references by these [17, 18] and other [10, 19] authors, relies on a single parameter to aim complete fields of heliostats. Because of the close relation between k aiming factor and spillage losses, the preliminary objective of the present work is to provide a thorough analysis on the influence of k factor on flux profiles and, ultimately, on spillage losses.

Recent research evidences that uniform flux distribution in receiver tubes plays a key role in reducing the peak thermal stress [20], which is the most limiting factor in the most irradiated receiver panels [17]. In this respect, the main purpose of the work is to formerly find the flattest possible flux distributions, objective for which the symmetric aiming methodology is adopted.

The manuscript is structured as follows. First, for a single heliostat it is defined the aiming factor in order to estimate the size of the beam and consequently point the heliostat. Dunhuang SPT plant, case study used throughout this work, is introduced in Section 3. Section 4 analyzes the effect of the aiming factor approach on the receiver spillage. For the whole field of heliostats, symmetric aiming is applied in Section 5. And Section 6 explores the aiming to achieve uniform flux profiles. At the end, the Appendix describes the flux map shifting procedure.

The flux distributions by heliostat fields have been computed with the convolution-projection method reported in Ref. [16] and experimentally validated in Refs. [16, 21]. The resulting in-house software FluxSPT is available for free download from the link in Ref. [22]. FluxSPT currently contains three existing SPT plants of moderate, medium and large size, namely: Dunhuang, Gemasolar and Crescent Dunes.

2. Aiming factor

The proposed aiming strategy is based on a single parameter, k, named aiming factor. For a single heliostat, this Section describes: first, the estimation of the beam size as a function of k factor; and, then, the determination of the aim point. This aiming strategy is implemented in the FluxSPT software tool [22].

2.1. Beam radius

The present aiming strategy relies on a proper estimation of the size of the beam incident on the receiver. In principle, a particular size cannot be defined for the beam reflected by a heliostat. In the following, it is introduced a calculation procedure on the basis of k aiming factor.

The flux density distribution on the image plane produced by a focusing heliostat follows an essentially circular Gaussian distribution with effective standard deviation σ_e. This evidence, supported by measurements and MCRT simulations, is inherently included in well-known convolution models as: UNIZAR [23], DELSOL [24] and HFLCAL [25].

Herein, it has been adopted the analytic function on the image plane by UNIZAR, where the effective standard deviation (σ_e) results from the convolution of sunshape (σ_{sun}), mirror slope (σ_{slp}), and tracking (σ_{trk}) errors. In the effective error equation, ω_h stands for the incidence angle on the heliostat.

$$\sigma_e = \sqrt{\sigma_{sun}^2 + 2\left(1 + \cos\omega_h\right)\sigma_{slp}^2 + \sigma_{trk}^2} \qquad (1)$$

By analogy with a circular normal distribution, 68%, 95% and 99.7% of the total flux is within the cone of aperture angle from heliostat center equal to σ_e, $2 \cdot \sigma_e$ and $3 \cdot \sigma_e$, respectively. Therefore, it can be defined a factor k, generally ranging between 0 and 3, that gives an idea on the energy that lies within $k \cdot \sigma_e$, in line with the 68-95-99.7 rule for normal distribution.

The radius of the beam (BR) on the image plane (si), that normal to the main reflected ray (or $\mathbf{t}$ target vector), is derived from the cone geometry. For a given SR slant range (distance from the heliostat to the receiver), the beam radius is function of the k factor, as declared in Eq. 2. Obviously, the higher the k value, the larger the estimated beam circle is.

$$BR_k^{si} = SR \cdot \tan\left(k \cdot \sigma_e\right) \simeq SR \cdot k \cdot \sigma_e \qquad (k \cdot \sigma_e << 1 rad) \qquad (2)$$

Fig. 1 displays the flux distribution produced by a heliostat in both a 3D view (left) and a 2D view (center), as well as the vertical profile through the

target point (right). Red circles outline the beam circumferences for three k values: 1, 2 and 3. Instead of flux density, F, in W/m², the distribution is quantified in concentration ratio of flux density, C, taking advantage of its independence of instantaneous direct normal irradiation, DNI. The concentration ratio of flux density is dimensionless, as derived from Eq. 3, while also can be expressed as the number of instantaneous suns focusing on the receiver.

$$F = C \cdot DNI \tag{3}$$

The flux distribution on the image plane is shown in Fig. 1a. The red circles are the beam boundaries for $k = 3, 2, 1$, whose radii are estimated with previous Eq. 2.

On the surfaces of the receiver, the flux distribution is projected from the image plane, following the procedure of the optical model, that is detailed in Ref. [16]. Similarly, the beam circumference is projected on the receiver panels, which is equivalent to the intersection of the cone of light with the receiver. The flux distribution on the half visible side of the receiver is shown in Fig. 1b.

For aiming strategy purposes, the beam size on the vertical of the receiver is only needed. The radius of the beam in vertical direction as a function of k factor, BR_k, can be easily calculated from that on the image plane BR_k^{si}. Known the elevation angle of the target vector (ϵ_t), Eq. 4 estimates the beam radius depending on k factor.
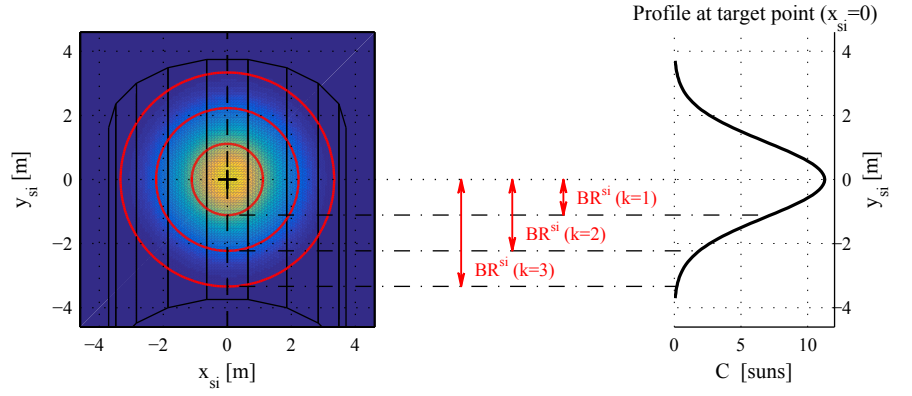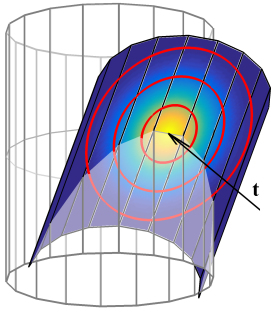
$$BR_k = \frac{BR_k^{si}}{\cos \varepsilon_t} = \frac{SR \cdot k \cdot \sigma_e}{\cos \varepsilon_t} \tag{4}$$
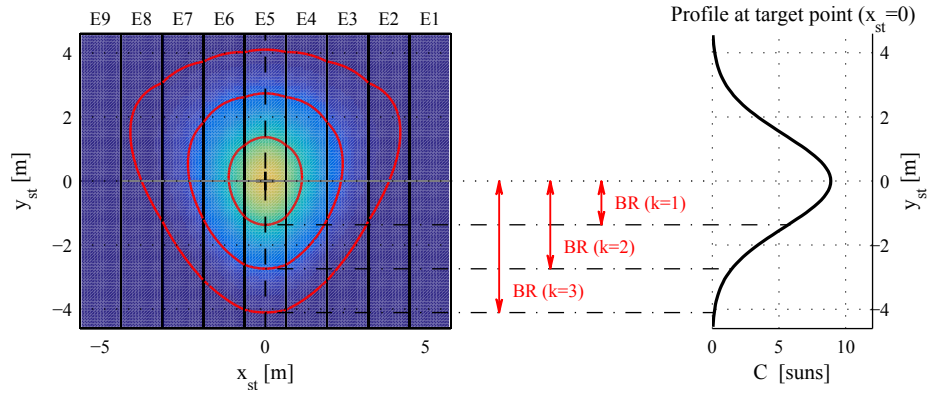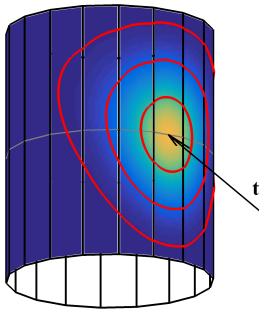
2.2. Targeting

Once the beam radius has been estimated as a function of the aiming factor, the heliostat is targeted in such a way that the beam is tangent to either the lower or the upper edge of the receiver. In other words, the heliostat is pointed at a vertical distance BR_k from one of the edges.

For the sample heliostat used in the preceding Subsection, Fig. 1c illustrates the concentration map that results from applying $k = 2$. In this example, the beam is tangent to the bottom receiver edge.
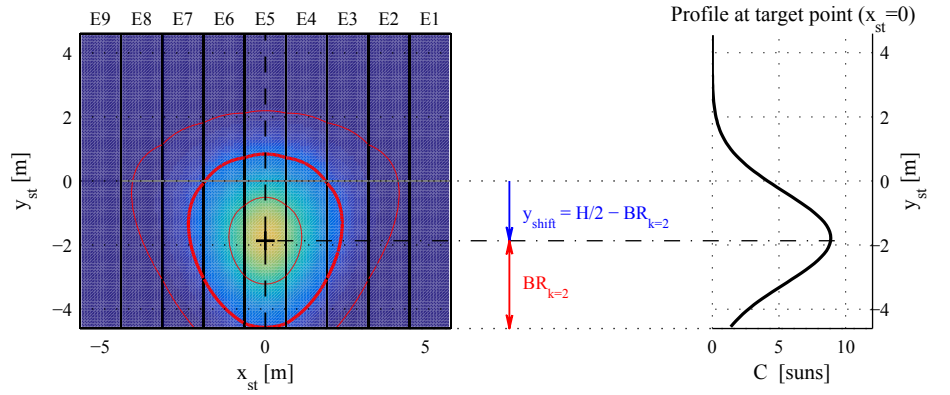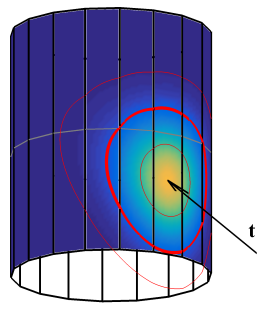
This targeting procedure entails the adjustment of the target point along the vertical direction on the receiver surface. To minimize lateral spillage losses in cylindrical receivers, the azimuth of the aim point is that of the pointing heliostat; i.e. the target vector is coplanar with the vertical axis of

6

Profile at target point ($x_{si}=0$)

BR^{si} (k=1)
BR^{si} (k=2)
BR^{si} (k=3)

y_{si} [m]
x_{si} [m]
y_{si} [m]
C [suns]

t

(a) On image plane.

Profile at target point ($x_{st}=0$)

E9 E8 E7 E6 E5 E4 E3 E2 E1

BR (k=1)
BR (k=2)
BR (k=3)

y_{st} [m]
x_{st} [m]
y_{st} [m]
C [suns]

t

(b) On receiver surface.

Profile at target point ($x_{st}=0$)

E9 E8 E7 E6 E5 E4 E3 E2 E1

$y_{shift} = H/2 - BR_{k=2}$

$BR_{k=2}$

y_{st} [m]
x_{st} [m]
y_{st} [m]
C [suns]

t

Image at summer solstice noon
by Dunhuang heliostat in 7$^{\text{th}}$ row, east azimuth.

(c) Targeting for $k = 2$.

Figure 1: Flux distribution and beam boundaries (in red) for several aiming factors $k = 3, 2, 1$.

the receiver/tower. Thus, vertical shifting is only considered, in contrast to horizontal shift which is not supported.

Whether the beam diameter, given a k factor, is greater than the receiver height (H), equatorial aiming is kept; on the contrary, spillage losses would unwillingly increase. The vertical shifting of the aim point respect to the equatorial target point (y_{shift}) is accordingly summarized in the following Equation. The minus sign applies for aiming tangent to the lower edge, otherwise the shift is upwards.

$$y_{shift} = \begin{cases} \pm \left(\frac{H}{2} - BR_k \right) & if \ BR_k < H/2 \\ 0 & if \ BR_k \geq H/2 \end{cases} \tag{5}$$

Since the beam size decreases with k aiming factor, then the lower the k factor, the higher the vertical shift is. This is why parameter k has been named aiming factor.

3. Case study

The methodology presented in this paper is valid for any SPT plant with central cylindrical receiver. As case study to illustrate the procedure and to show results, it is considered Dunhuang SPT plant. This is a 10 MW$_e$ plant located in China at 40.08° north latitude.
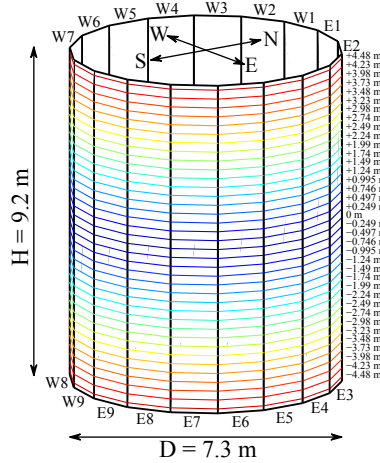

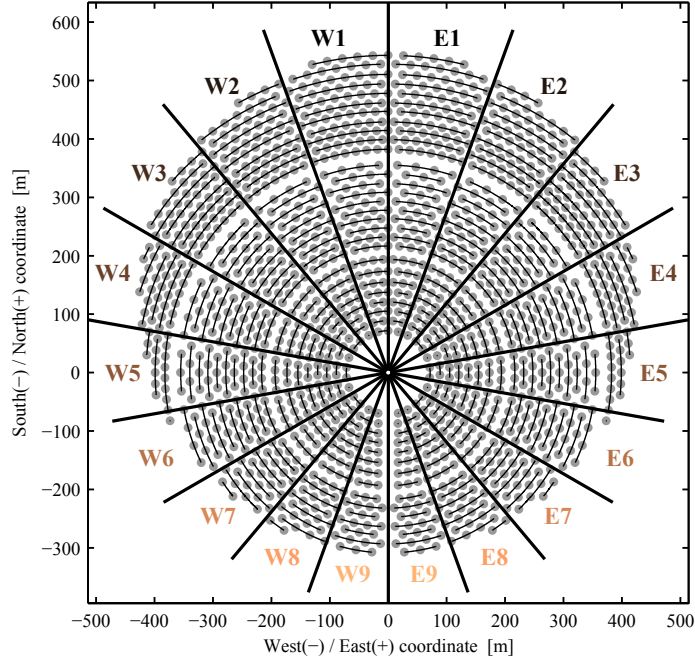Figure 2: Dunhuang receiver geometry and aim levels under consideration.

Figure 3: Heliostat field layout of Dunhuang with divisions by sector.

The receiver, 9.2 m in height and 7.3 m in diameter, comprises 18 panels, and stands at the top of the tower, being 121 m its optical height. Fig. 2 depicts the receiver, where the panels are labeled according to their orientation (East or West), and numbered from the north. Aim levels to be considered are also marked with colored lines in the Figure.

The field consists of 1525 square heliostats of 115 m^2 mirror surface each. Fig. 3 depicts the heliostat field layout, and its division in sectors according to their target panels.

For the evaluation of the effective error (Eq. 1), a reliable value of sunshape standard deviation equal to 2.09 mrad has been taken [26, 27]. A common error of 2.6 mrad is handled for the mirror slope error, while the tracking error is neglected since it does not produce any actual modification on the flux distribution by the heliostat.

4. Effect on spillage

This Section analyzes how the above described aiming factor approach affects the receiver spillage. Actually, k parameter not only determines the

9

target point of each heliostat in a field, but also gives some idea of the magnitude of the spillage losses, or its complimentary, the receiver interception.

Spillage losses are quantified by the spillage factor (f_{sp}), also known as intercept factor. This loss factor is the fraction of direct solar flux reflected by the heliostat that is actually intercepted by the receiver. In terms of the concentration ratio in each node of the receiver, $C_{i,j,p}$ in receiver mesh node coordinates, the spillage factor can be computed with the following Equation [16], where: AC stands for the area of the cells in the receiver mesh, and AM is the mirror area of the heliostat.

$$f_{sp} = \frac{\sum\limits_{i,j,p} C_{i,j,p} \cdot AC}{\cos \omega_h \cdot AM} \tag{6}$$

In the following examples, the equinox day at solar noon time is considered. Fig. 4 shows the spillage factors of the heliostats in Dunhuang field at equinox noon for equatorial aiming, and taking aiming factors equal to 2, 1 and 0. In this example, every single heliostat is targeted so that the beam circumference, whose radius is computed with Eq. 4, is tangent to the bottom edge of the receiver; what is termed downwards aiming in the following. Half of the field is displayed because of symmetric situation at solar noon.

Evidently, as the aiming factor decreases the spillage losses increase. As shown in the Figure, receiver interception for $k = 2$ is only very slightly lower than with equatorial aiming. Indeed, aiming with $k = 3$ is equivalent to equatorial aiming for Dunhuang SPT plant.

From the basics of the proposed aiming strategy, a given aiming factor would produce the same spillage losses for all the heliostats in a field. This fact is noticeable for small aiming factors, but not fully for high k values; where the spillage colormap is not completely uniform in Fig. 4. Beam spots greater than the receiver size in distant heliostats justifies spillage factors smaller than 1, even for equatorial aiming.

A more detailed analysis on the influence of the aiming factor on the spillage losses is provided in Fig. 5 for selected heliostats, specifically those circled in black in previous Fig. 4. The Figure depicts both the cases of downwards and upwards aiming, in respectively solid and dashed lines.

For twelve heliostats in row 11, Fig. 5a represents k $vs.$ f_{sp}, where is again evidenced that the lower the k factor, the higher the spillage losses are. At equinox noon in Dunhuang plant, given a k value, the spillage losses are moderately constant, regardless of the heliostat azimuthal position.
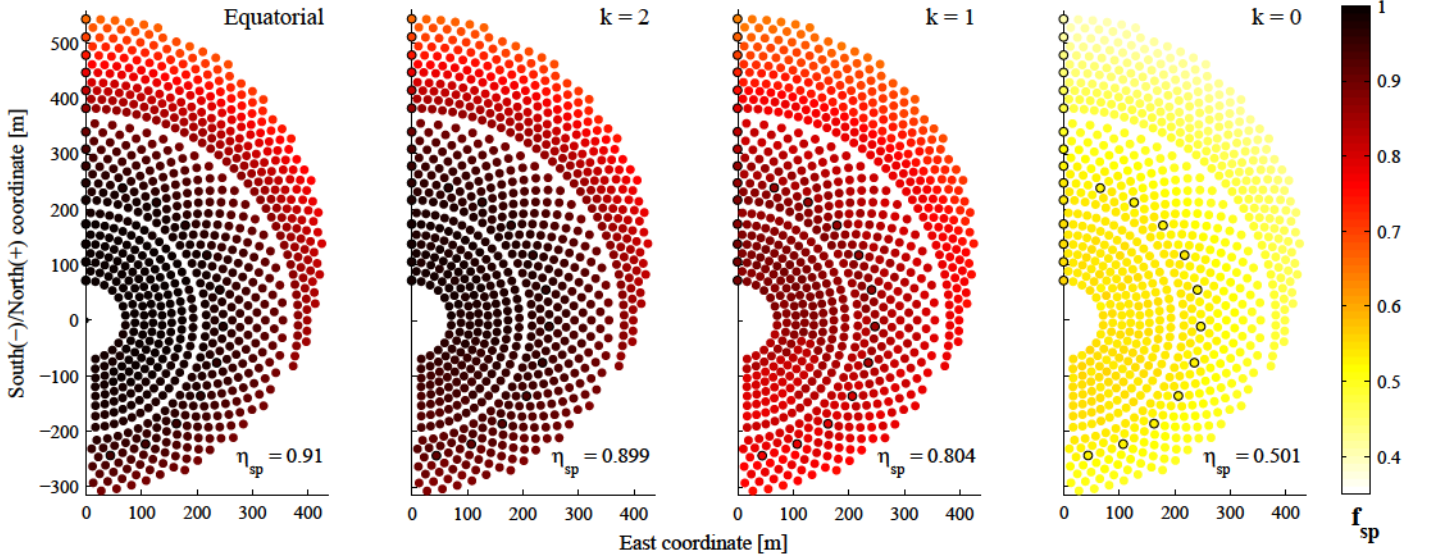
10

Figure 4: Heliostat spillage loss factors in Dunhuang field (east half) at equinox noon for equatorial aiming, and aiming factors: 2, 1 and 0. Beams tangent to bottom receiver edge (downwards aiming).

Fig. 5b similarly represents the cases of fifteen heliostats in the north axis. Given a k value, now the spillage losses are diverse depending on the heliostat distance to the tower. From mid-distance rows to last ones, it is noticed that the farther the heliostat, the higher the spillage loss is. This amplitude is remarkable for high aiming factors, because of the larger beam sizes for last rows compared to the receiver size. As can be seen in the Figure, the spillage loss is maximum (flat top) from a k value onward; such situation points out that equatorial aiming is taking place. Dash-dot line in Fig. 5b demarcates the equatorial aiming area.

From Fig. 5 it is concluded that the progression of spillage losses as a function of the aiming factor follows a rather logarithmic profile. Whether a discrete sweep of k factors is performed (e.g. in Subsection 6.2 to determine flat flux profiles), a logarithmically spaced scan of k would roughly lead to constant steps in the spillage losses; as well as in the aim point shifting.

By comparing for a given heliostat and k factor, both downwards and upwards aiming in Fig. 5, respectively in solid and dashed lines, downwards aiming results in higher interception efficiency; except for equatorial aiming or high k values, where both tend to match. Even though the beam is placed

11

(a) Heliostats with azimuth 180 (north axis) in odd rows.
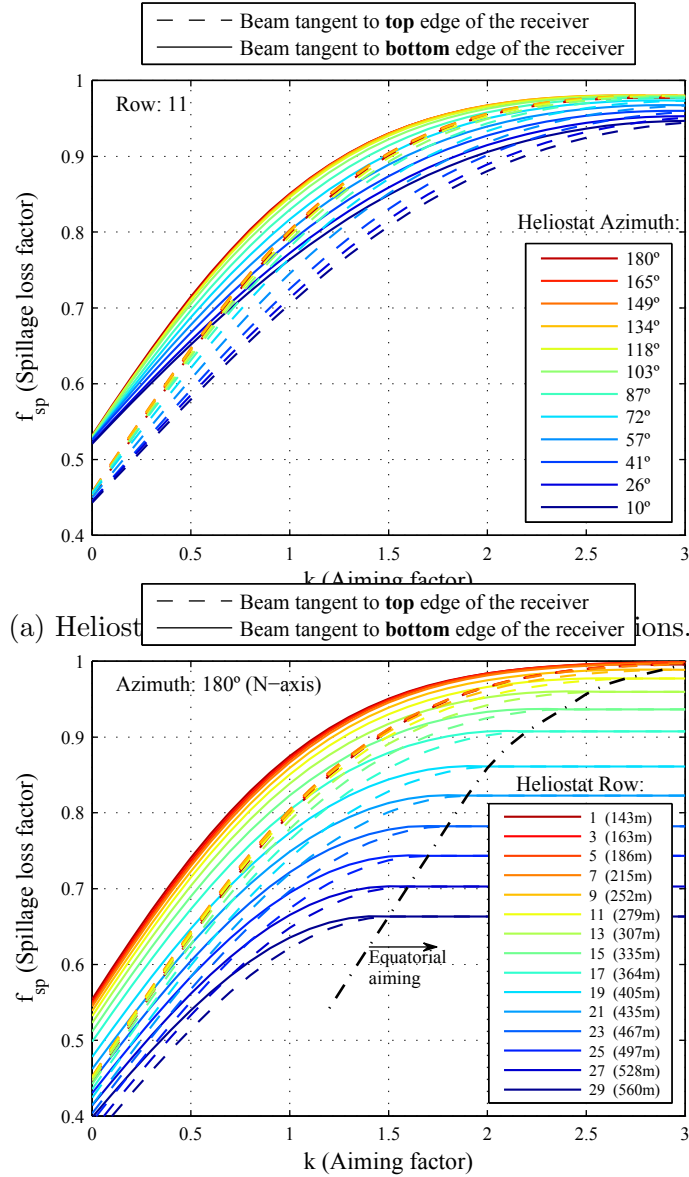
(b) Heliostats with azimuth 180 (north axis) in odd rows.

Figure 5: Spillage loss factor of selected heliostats in Dunhuang plant at equinox noon depending on aiming factor. The selected heliostats are circled in black in Fig. 4. Solid and dashed lines correspond to respectively downwards and upwards aiming.

tangent to the receiver border (bottom or top) in both cases, since the helio-
stat reflected beam follows an ascending direction, receiver panels adjacent
to the target one are on average reached above the aim level. Hence, receiver
interception is smaller when upwards aiming is set. This is also evident in
the spillage efficiency of the whole heliostat field (η_{sp}), from inspection of
upwards and downwards outputs in Table 1.

5. Symmetric aiming

5.1. Methodology

From a whole field of heliostats, symmetric flux maps about the receiver
equator can be achieved by alternatively aiming each row of heliostats up-
wards and downwards. Such approach was formerly proposed by Vant-Hull
in Ref. [15].

In the present study, even rows of heliostats aim tangentially to the bot-
tom receiver edge (downwards), while odd rows aim to the top edge (up-
wards). This symmetric aiming strategy is graphically depicted in Fig. 6,
where not only the resulting flux map, but also the aiming points are sym-
metric about the receiver equator. The summation of the flux maps from
upwards (odd rows) and downwards (even rows) aiming leads to a nearly
symmetric flux map.

The symmetric aiming procedure illustrated in Fig. 6 is provided for the
Dunhuang case study, considering equinox day at 8:00 solar time. Aiming
points and flux map have been computed for an aiming factor equal to 1.5 in
all the heliostats of the field. Parallel projection between neighbor heliostats
has been utilized in the calculation of shading and blocking losses.

The determination of aim points from a given k factor, following the
procedure described in Subsection 2.2, results in a continuous space of aim
levels. To simplify the control of the heliostat field, it is generally defined a
discrete number of aim levels on the receiver. Then, each and every heliostat
is pointed to the aim level whose distance to the equator is immediately
below the vertical shift computed with continuous Eq. 5; which can be called
shifting quantization. It becomes clear that the higher the number of aim
levels, the more possibilities of aiming exists and flatter flux profiles are
achievable.

For the Dunhuang case study, it has been considered 37 aim levels; an odd
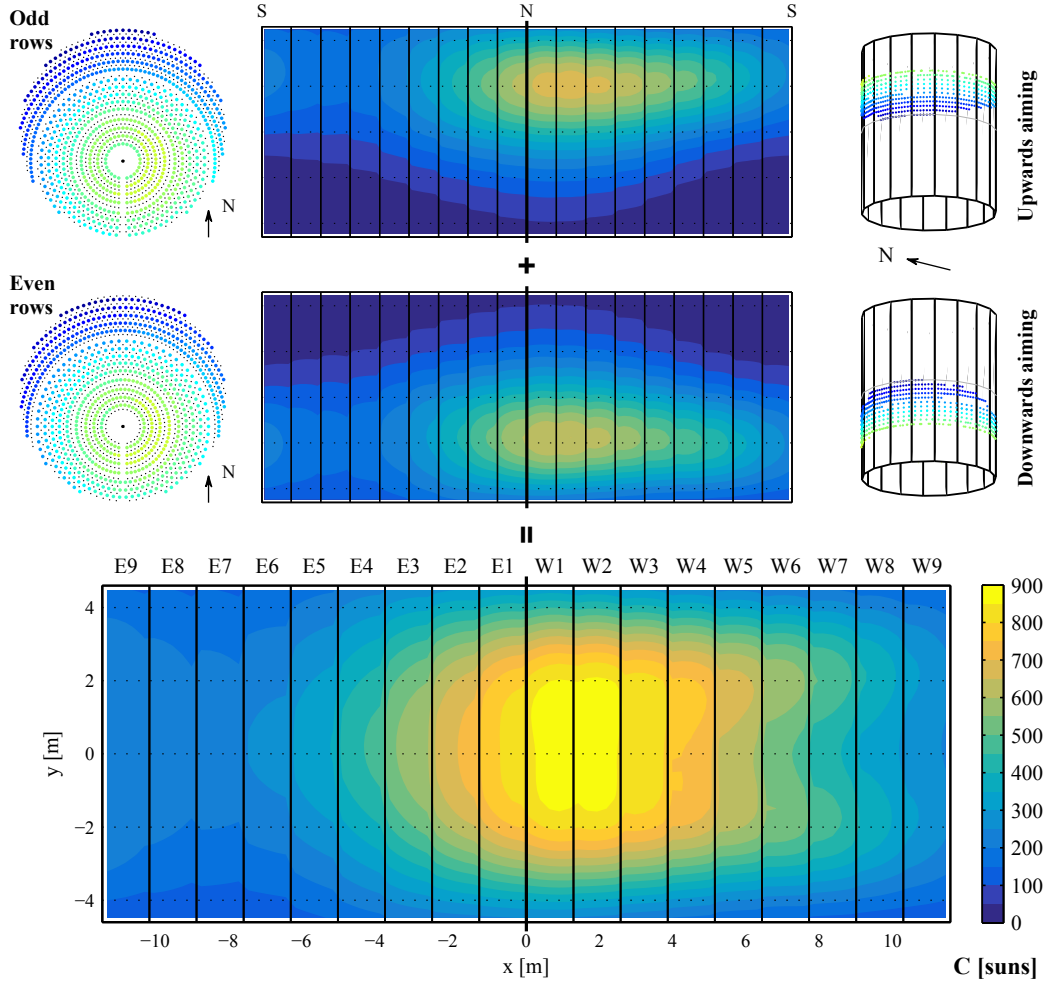number is required to attach the aim level in the middle to the equatorial

Figure 6: Symmetric aiming strategy procedure. Example for Dunhuang plant at equinox 8:00 solar time given $k = 1.5$.

line. Fig. 2 represented, in the 18-panels Dunhuang receiver, the 37 aim levels colored for identification in heliostat field plots of aim points.

In this instance, the aim levels match the receiver mesh where the flux distribution is computed. This way, or taking a vertical discretization that is submultiple of the distance between aiming levels, is advantageous for the flux map shifting procedure reported in Appendix A.

5.2. Case study results

For Dunhuang at equinox noon, Fig. 7 illustrates the maps of concentration ratio in the west receiver panels for aiming factors equal to: 3, 2, 1, and 0; keeping the same colormap scale for proper comparison. In the right side of the Figure, the mean vertical concentration profiles for each west panel is drawn according to the panel color coding at the top of the maps. In the left, the west side of the field is colored by the aim level of each heliostat, following the color levels in previous Fig. 2, which again have been slightly marked at the right side of the flux map.

Concentration map for $k = 3$, which is equivalent to equatorial aiming in Dunhuang case study, has a remarkable hot strip in the equatorial belt, reaching a peak concentration of 1683 suns in the most irradiated panel (W1). On the contrary, for $k = 0$ two peaks (up to 863 suns) emerge in the receiver edges, which is a very inefficient aiming with less than 50% interception; see Table 1.

Aiming factors between the extremes, i.e. 1 and 2, leads to flux maps also in between. For $k = 1$ in Fig. 7, the two shoulders on the vertical profiles have just appeared. Meanwhile, $k = 2$ generates a single peak, definitely smaller than with $k = 3$, of 1372 suns in panel W1. However the average concentration ratio in the whole receiver is 559, slightly smaller than the 569 suns with $k = 3$.

From the inspection of the flux profiles, it can be noted not only the decreasing peak alongside the panels, but also the changing pattern depending on the aiming factor. One may predict that an aiming factor between 1 and 2 should lead to the flattest profiles.

Table 1 summarizes the spillage efficiency of Dunhuang field at equinox noon for several aiming factors ranging from 3 to 0. With symmetric aiming, η_{sp} is in between the values for unfeasible upwards and downwards aiming. Since the 68-95-99.7 rule for normal distribution was taken as the starting point for the aiming factor strategy (Subsection 2.1), the probability for Gaussian distribution in correspondence with k is displayed in the last two columns of the Table. Even though η_{sp} and Gaussian probability exhibit the same trend, it is obvious that intercept efficiency is around 50% for $k = 0$ in contrast to 0% probability for $0 \cdot \sigma$. Nonetheless, the flux distribution from the heliostats is clipped by the finite apparent shape of the receiver.
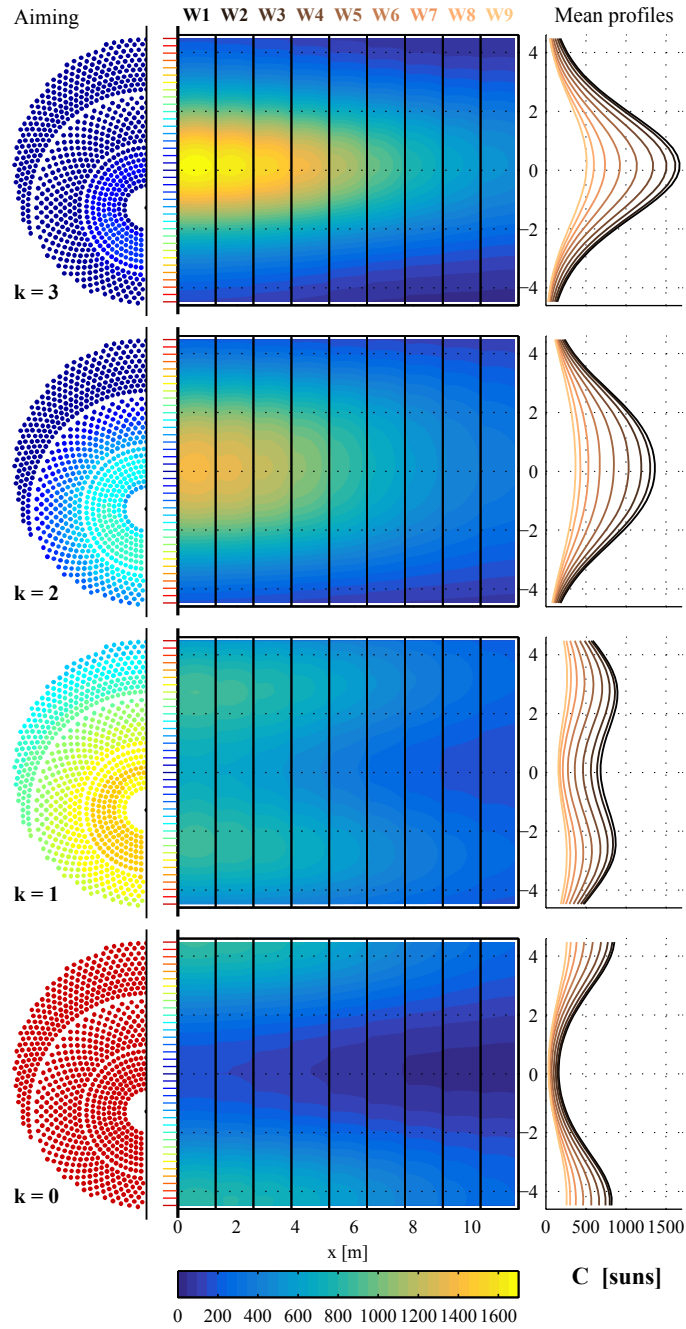
15

Figure 7: Maps of concentration ratio in west panels of Dunhuang receiver at equinox noon, for aiming factors equal to: 3, 2, 1, and 0. Right: Mean vertical profiles for each panel. Left: aim level for each heliostat in the field.

16

Table 1: Field spillage efficiency in Dunhuang at equinox noon for different aiming factors and considering: upwards, downwards, and symmetric aiming.

| Aiming | | $\eta_{\mathbf{sp}}$ [%] | | | Normal dist. | |
		Upw.	Sym.	Dow.	Prob.[%]	Range
	Equatorial		91.0		100.0	∞
	3	90.9	91.0	91.0	99.7	$3 \cdot \sigma$
	2.5	90.3	90.5	90.7	98.8	$2.5 \cdot \sigma$
	2	88.6	89.1	89.7	95.5	$2 \cdot \sigma$
k	1.5	84.0	85.2	86.5	86.6	$1.5 \cdot \sigma$
	1	74.6	76.8	79.0	68.3	$1 \cdot \sigma$
	0.5	60.5	63.4	66.4	38.3	$0.5 \cdot \sigma$
	0	43.7	46.8	50.1	0	0

6. Flat distribution

From the effect of different aiming factors in the symmetric aiming strategy, it can be concluded that there might be a k_{flat} factor where the flux distribution would be the flattest possible. In fact, given a solar position, rather than a single k_{flat} for the whole field, it can be found an specific one for each sector/panel, as described in the following.

6.1. Aiming by field sectors

The field of heliostats is divided in sectors in accordance with the target panel. Since only vertical shifting of aim points is considered, the aperture angle of the receiver panels bounds the field sectors. So that in the 18-panels Dunhuang receiver, the angle of each sector is 20°. In previous Section 3 Fig. 3 represents the 18 field sectors, which are labeled according to their target panel. The heliostats in each row-sector are linked with arc lines in that Figure.

Distinct aiming factors for each field sector can now be defined. Then, given a k_{sector} value in a field sector, the heliostats in the same row-sector will point to the same aim level. This is explained by the almost identical beam size for the heliostats in a row-sector (Eq. 4), that, from Eq. 5 and shifting quantization, finally results in the same aim level.

To ensure that all the heliostats in a row-sector point to the same aim level, the beam size may be computed in two alternative ways. First, it could

be considered the quadratic mean of the heliostats beam radii in such row-sector. This approach was used in Ref. [17], but the correspondence between aiming factor and spillage losses, as analyzed in previous Section 4, is lost. Second, it is more appropriate to compute the beam size as the mean beam radius of the heliostats in the row-sector, as considered in the present study.

6.2. Flat aiming factors: k_{flat}

This Subsection describes the procedure to determine k_{flat}; that is: the aiming factor for each field sector in order to procure the flattest distribution using the symmetric aiming strategy.

The purpose of finding k_{flat} is worked out by an algorithm that seeks along a sequence of k factors for those providing the flattest vertical profiles in each receiver panel. Since the flux distribution in each panel is mainly affected by the heliostats in its field sector, the search is performed sector-by-sector. And, at the end, considering the contribution of the whole heliostat field, it is checked that the vertical flux profiles are still kept flat.

The success of the algorithm depends on a proper selection of the sequence of k values to be swept. From the analysis in Section 4, it has been concluded that spillage losses logarithmically increase with the aiming factor. There-fore, a sequence of logarithmically spaced k factors would result in roughly constant steps in the spillage losses. On the other hand, the number of k values in the sequence should be such that nearly all aim levels were swept. It has been found that a series of around half the number of aim levels (37 in this instance), performs a regular scanning. Hence, in the Dunhuang case study 18 bins have been considered. Selecting $k = 3$ (equatorial aiming) and $k = 0.5$ (almost edge aiming) as upper and lower bounds of the sequence, the whole series is: 3.00, 2.72, 2.46, 2.23, 2.01, 1.82, 1.65, 1.49, 1.35, 1.22, 1.11, 1.00, 0.91, 0.82, 0.74, 0.67, 0.61, 0.55, 0.5.

To find out the k_{flat} of each sector, it is computed in each panel the vertical profiles resulting from each k factor following the sequence. The latest aiming factor before obtaining two peaks in the profile, is finally the k_{flat} for such sector. This algorithm is similar to the sweep routine employed in Ref. [17].

For the Dunhuang case study in the equinox day at 8:00 solar time, Fig. 8 represents the vertical profiles of C concentration ratio for each panel in the receiver. Each grayscale profile corresponds to a k value in the sequence, as labeled in the color legend at the right side of the Figure. The red thick line in each panel identifies the flattest profile and its corresponding k_{flat} factor.
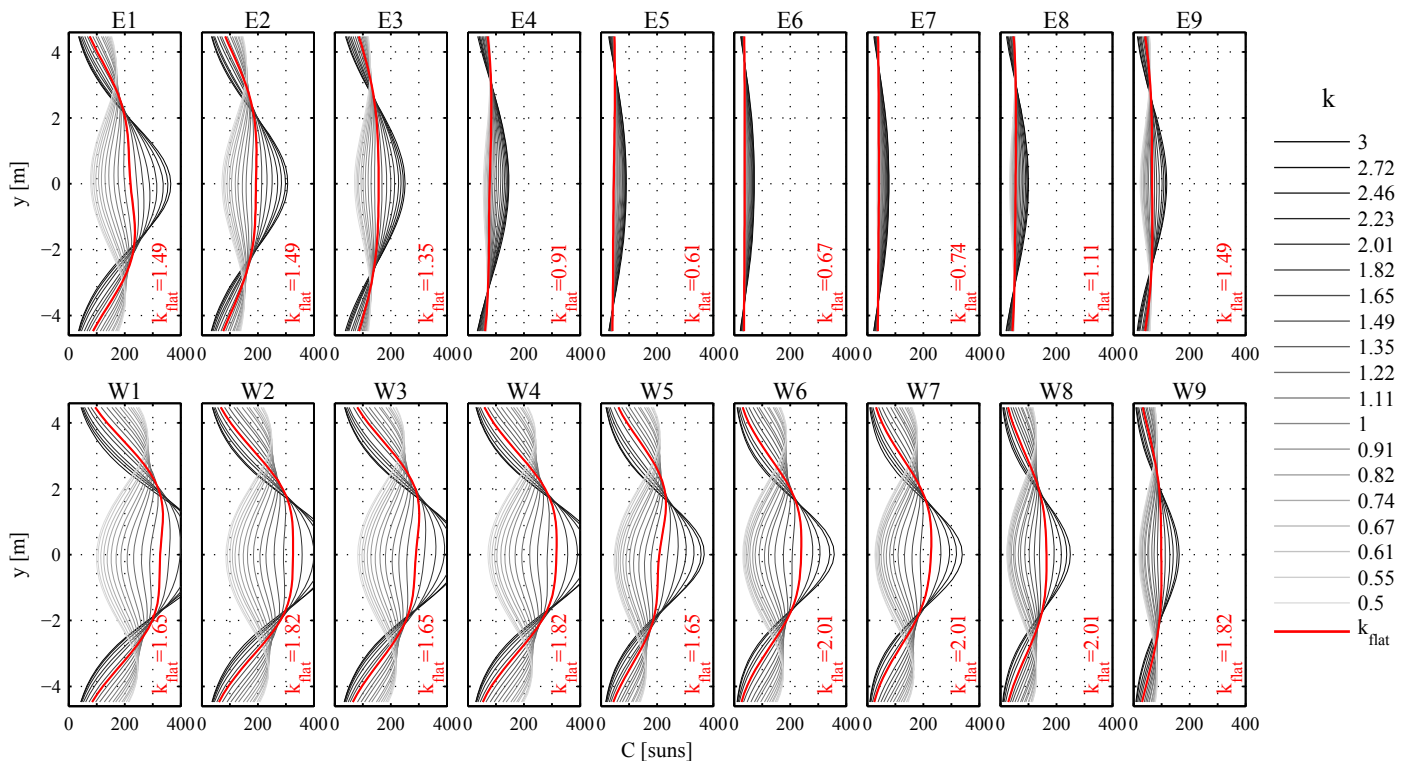
18

Figure 8: Vertical profiles of concentration ratio in each receiver panel of Dunhuang at equinox 8:00 solar time, for aiming factors ranging from 3 to 0.5 (sweep). Red thick curves represent the flattest profile for each panel, achievable with k_{flat}.

As can be seen in Fig. 8, the profiles for k values smaller than k_{flat} have a central valley and two peaks towards the edges, so that spillage losses gradually increase. On the contrary, aiming factors higher than k_{flat} lead to a central peak and high gradients along the receiver vertical direction.

The convolution-projection method used to compute the flux distribution [16] is faster than MCRT simulations. However, in computationally intensive procedures such as aiming optimization [17] or the current sweep algorithm, where diverse aiming configurations are required, significant time can be saved using the flux map shifting approach described in Appendix A. The freeware FluxSPT tool [22] also takes advantage of the mesh shifting to instantly compute the flux maps resulting from different aiming factors.

For the flux profiles of each receiver panel in Fig. 8, from which the k_{flat} has been obtained, just only the corresponding field sector was aimed to

19
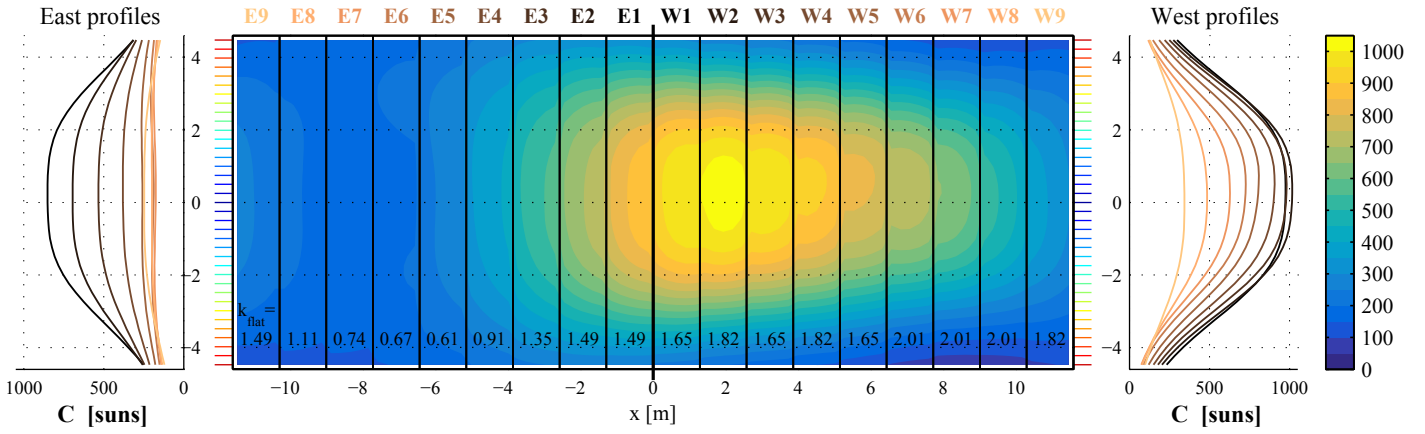
(a) Map of concentration ratio and vertical profiles.
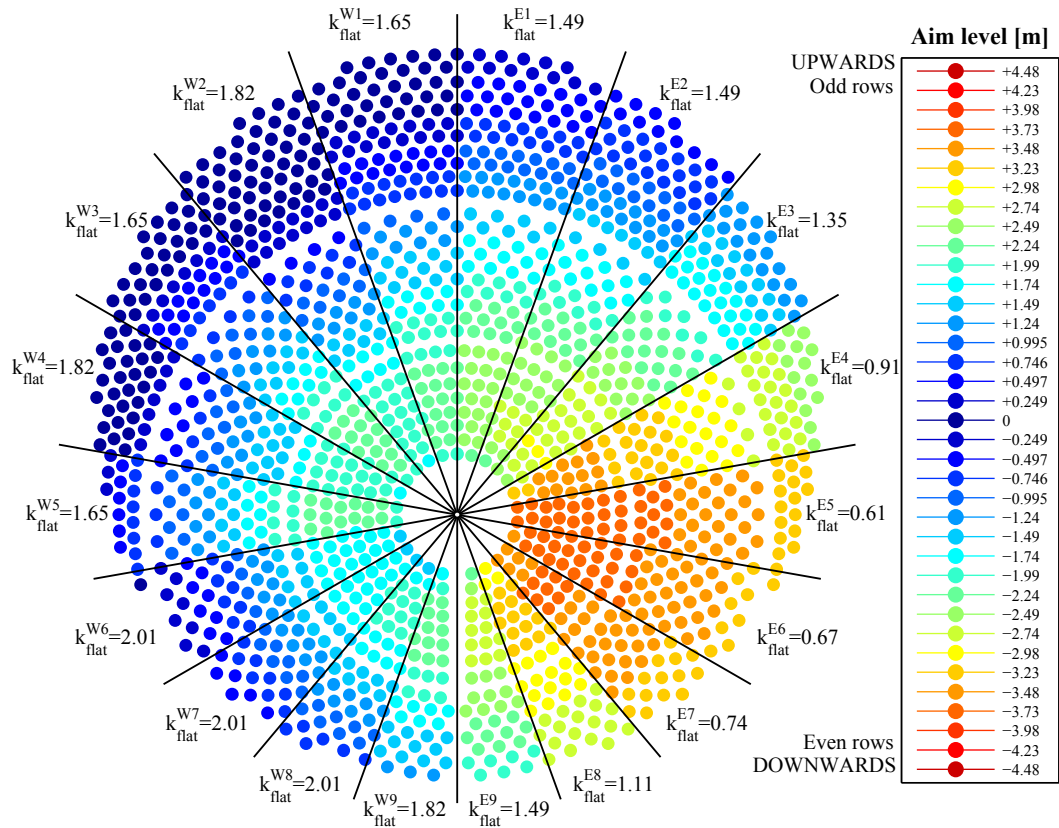
(b) Aim point level of each heliostat.

Figure 9: Dunhuang at equinox 8:00 solar time, using flat aiming factors k_{flat}.

the panel. By superimposing the flux distribution resulting from each sector k_{flat}, it is gained the whole *flattest* concentration map, reproduced in Fig. 9a. In the left and the right sides of the Figure, they are depicted the vertical profiles for the respectively east and west panels. From the inspection of Fig. 9a, it is noticed that the profiles resulting from the whole heliostat field are also flat in their central region; therefore, the sector-by-sector approach in the sweep algorithm to find out the k_{flat} values appears plausible.

On Dunhuang layout, Fig. 9b represents the aim point level for each heliostat, that leads to the flat distribution in Fig. 9a. For the equinox 8:00 case, the greatest aim point shifting about the receiver equator, identified by warm colors, takes places in the heliostats around the solar azimuthal location, specifically in sectors E5, E6 and E7. In fact, these three panels yield the lowest k_{flat} values: 0.61, 0.67 and 0.74, respectively. On the contrary, heliostats in the last rows of the anti-sun location are aimed to the equator, or close to it.

6.3. Case study annual results

Running the sweep algorithm along the year, it can be collected for any solar position the k_{flat} factor for each field sector that generates the flattest flux distribution using the symmetric aiming approach. On an azimuth and elevation diagram for Dunhuang, Fig. 10 displays for each east sector the k_{flat} using a grayscale contour map that designates the aiming factors in the sweep sequence. Red lines represent the sun path in the 21st of each month, identifying the solstices and equinoxes, and white dashed lines indicate the solar times. By means of Eq. 5 and shifting quantization of y_{shift} to the aim levels, from Fig. 10 it is ultimately gained the aim point level for all the heliostats in Dunhuang field in order to achieve the flattest possible flux distribution at any time.

In the northern E1 sector, the k_{flat} factor is fairly constant throughout the year. In the southern E9 sector, k_{flat} is quite uniform during a single day, but varies along the year, being highest in summer solstice and lowest in winter solstice. In the remaining sectors, it is noticeable the change of the flat aiming factor in the first hours of the day, from small k_{flat} values to higher ones around noon and in the afternoon. Although Fig. 10 only compiles the east sectors, by making the symmetrical about the noon vertical axis (i.e. zero azimuth) it is gained the k_{flat} for the analogous west panels.

In a similar way, Fig. 11 displays the maximum concentration ratio of flux density, C_{max}, in each east panel resulting from the application of k_{flat} aiming
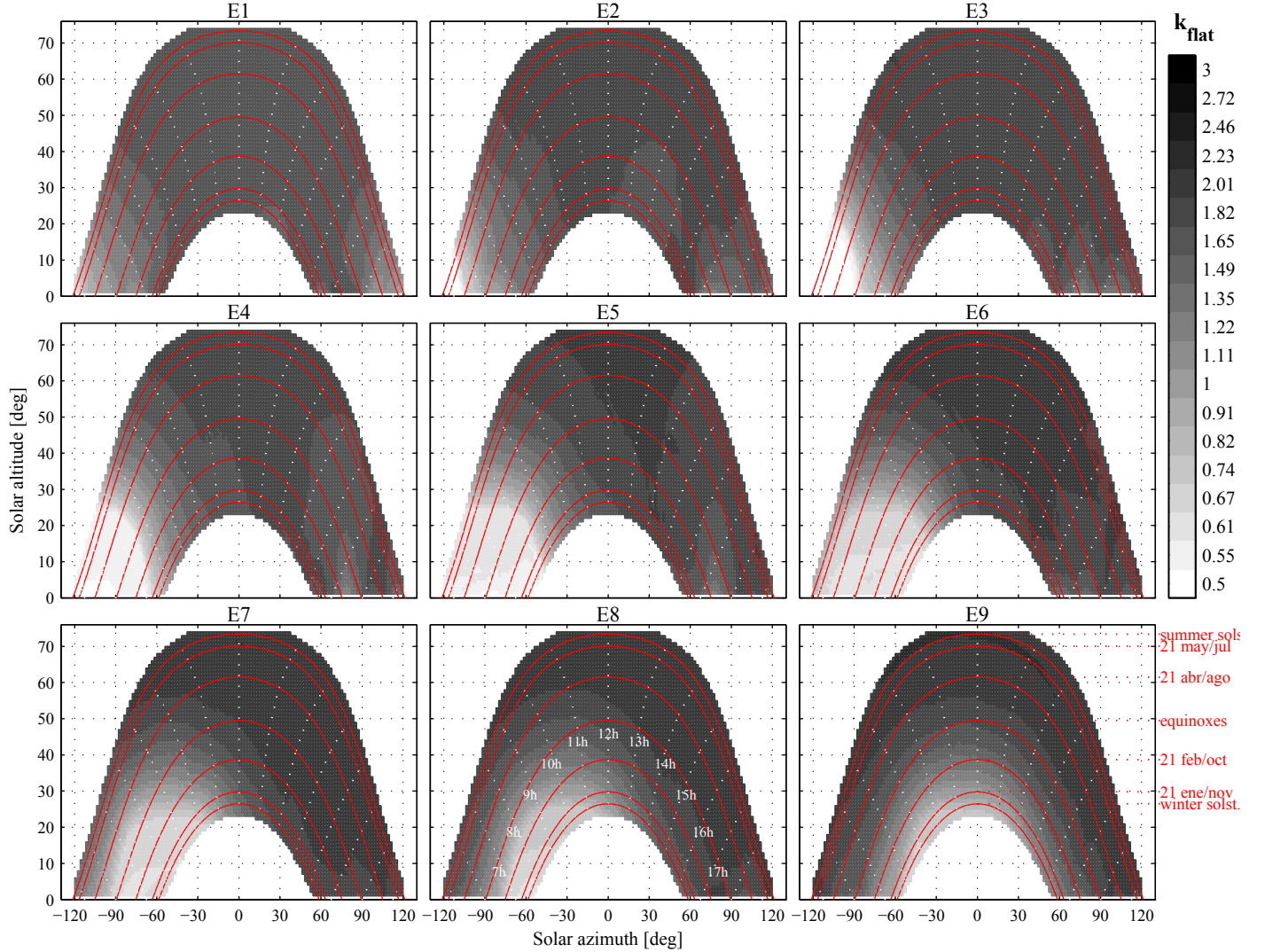
21

Figure 10: Flat aiming factors in Dunhuang plant for east sectors along the year (solar azimuth and elevation diagram).

factors. Therefore, such C_{max} is essentially the concentration ratio in the central region of the panel, where a flat vertical profile exists. As expected, the highest C_{max} values take place in the northern panels. Considering a particular panel, C_{max} is greater around noon than near sunrise and sunset.

Known the instantaneous DNI, from Fig. 11 and using Eq. 3 it is directly gathered the maximum flux density for each panel at any time. Whether
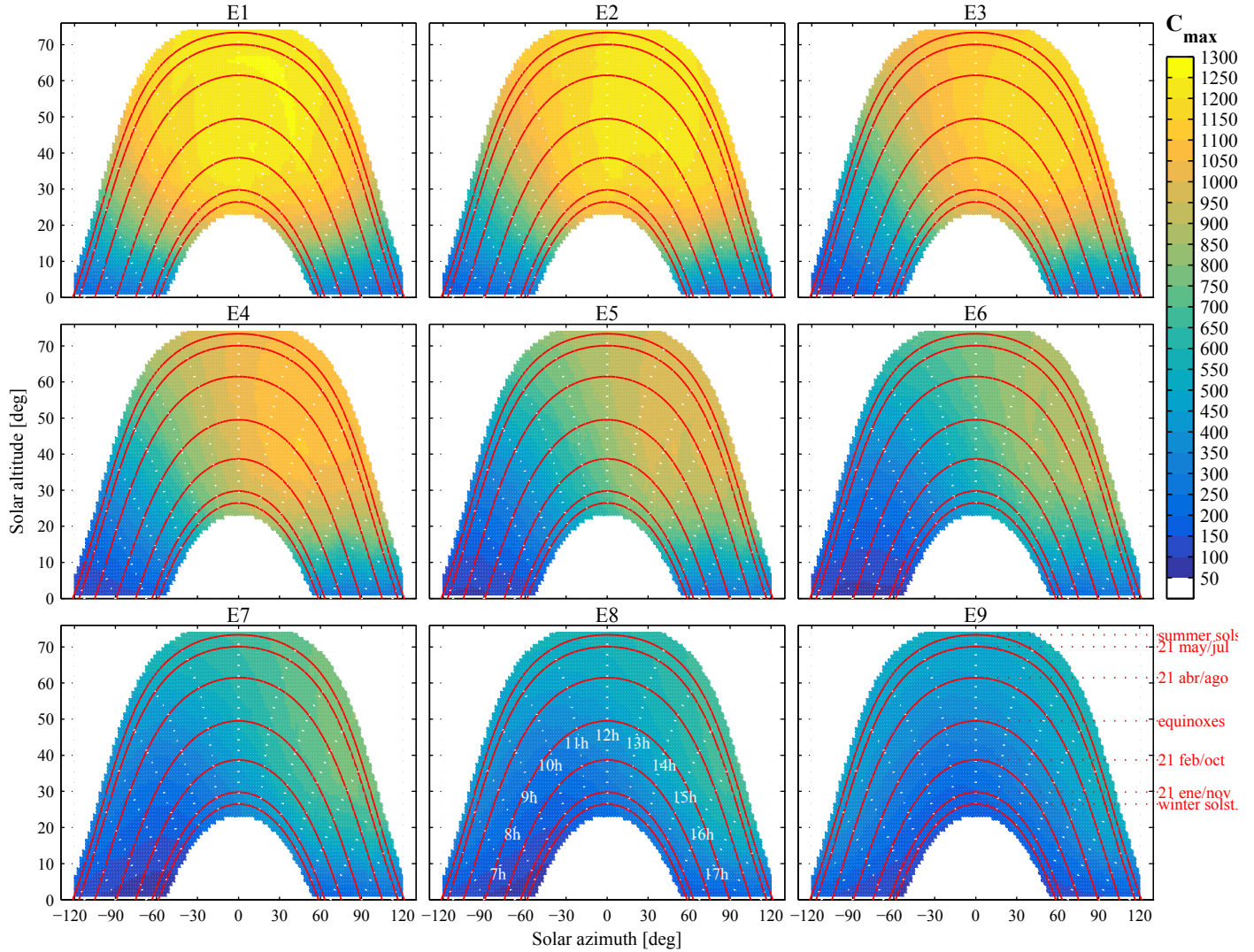
Figure 11: Maximum concentration ratios (using flat aiming factors) in Dunhuang plant for east receiver panels along the year (solar azimuth and elevation diagram).

limitations on the flux density exists, e.g. via Allowable Flux Density (AFD) [15, 17], it would be automatic to check such requirements. If, despite the flat symmetric aiming strategy, the AFD were exceeded, then an alternative aiming procedure, such as the fit algorithm in Ref. [17], could decrease the maximum flux at the expense of increasing spillage losses.

23

7. Conclusions

A symmetric aiming strategy has been developed to produce flux maps symmetric about the equator in cylindrical receivers. A plethora of flux distributions can be generated on the basis of a single parameter: k, ranging between 0 and 3 because of its analogy with Gaussian distribution probability. Equatorial aiming is commonly equivalent to $k = 3$, and $k = 0$ means alternatively aiming to top and bottom receiver edges. Aiming factors between the limits yield to symmetric maps also in between. This approach has been implemented in the software tool FluxSPT, available for free download from [22].

The k aiming factor serves to estimate the size of the beam reflected by each heliostat in a field, and then vertically shift to the target aim level so that the spots are alternatively tangent to either the upper or the lower edge of the receiver. It has been found that interception is logarithmically connected to k factor.

To reduce flux gradients and thermal stresses along the receiver tubes, a flat vertical profile is convenient. The k_{flat} values leading to the flattest possible symmetric flux maps have been deterministically found using a sweep methodology. This search becomes faster with the accurate enough mesh shifting procedure in the Appendix.

Taking advantage of sectorial division of the heliostat field in correspondence with the receiver panels, specific k_{flat} values have been provided for each sector, so that the flux profile is made flat in every single panel. For Dunhuang SPT plant in China, flat aiming factors for the whole year have been summarized in azimuth and elevation diagrams; k_{flat} is quite constant along the year except near sunrise and sunset, respectively in east and west field sectors.

Acknowledgments

Appendix A. Flux map shifting

The computation of the flux maps for each aiming factor, which is performed with the convolution-projection method in Ref. [16], in principle re-

24

quires an individual calculation for every aim point level considered. This
Appendix puts forward a methodology to quickly determine the flux distri-
butions by an heliostat pointing to any aim level in the receiver, given a
specific solar time. This procedure, which saves considerable computation
time in sweep and optimization routines, involves a negligible error com-
pared to direct, long-lasting, computation; as also justified at the end of this
Appendix.

The proposed methodology consists in computing only once the flux dis-
tribution by a heliostat, as in Ref. [16], considering equatorial aiming. Such
flux map is saved and, when a different aim level for the heliostat is required,
the original flux map is vertically shifted a distance equal to that between the
equator and the target level. Fig. 12 graphically illustrates this procedure,
which is implemented in the FluxSPT software tool [22].
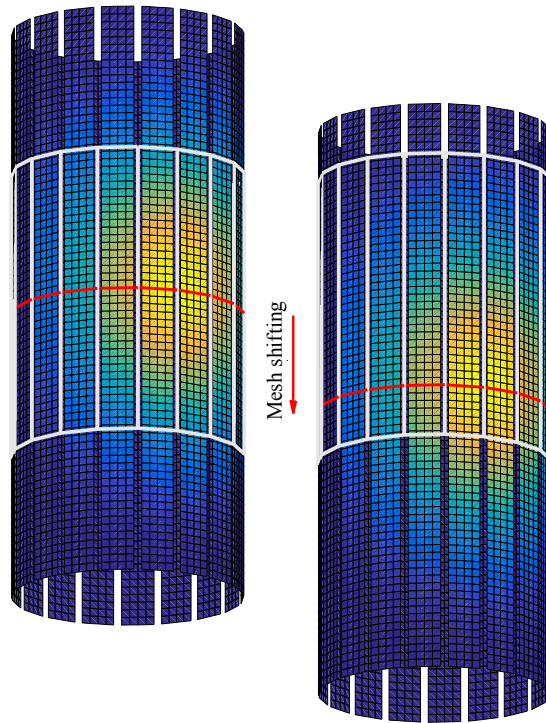
Figure 12: Graphical explanation of the flux map shifting procedure. Left: mapping on
extended receiver mesh for equatorial aiming. Right: mapping shifted downwards for a
given k-factor of 0.5. (Example at equinox noon for heliostat in last row, north azimuth).

Operationally, the flux map shifting procedure entails two issues to con-

sider. Firstly, the computational mesh in the receiver has to be extended beyond its upper and lower borders. Since the maximum shift would be half the receiver height ($k = 0$, edge aiming), the height of the full mesh might be twice the receiver height. This is shown in Fig. 12, where the receiver is highlighted by white lines.

Secondly, the computational mesh should match the predefined aim levels so that interpolation is favorably avoided. This can be achieved by taking a nodal spacing in the receiver mesh equal to, or submultiple of, the distance between aim levels. For instance, the 37 aim levels match the vertical discretization in Fig. 12, then the flux map shifts from the equator (red line in left image) to the target aim level (red line in right image).

Comparing the direct computation with the proposed flux map shifting procedure, very slight differences are found. For the extreme case of $k = 0$, Fig. 13 points out, for each heliostat in Dunhuang field at equinox noon, the associated error in the calculation of flux maps and spillage. The relative error in the spillage loss factor (east field side) is inversely proportional to the slant range, so that for far heliostats the relative error is around zero and for near heliostats almost 3%. In the west side of Dunhuang layout in Fig. 13, it is represented the root mean square deviation in the concentration maps, $RMSD(C)$, which is maximum in the near northern heliostats. This fact is explained by the highly concentrated spot resulting from the heliostats closest to the tower.

For the heliostat in the first row and north azimuthal position, Fig. 14 displays the concentration maps using both direct computation and flux map shifting, respectively in the eastern and western receiver panels. Even though the highest $RMSD(C)$ at noon takes place with that heliostat, the differences between both computation methods are insignificant; $RMSD(C) = 0.0445$ suns. It is concluded that computational cost can be saved with the flux map shifting procedure, which may be utilized in aiming optimization without meaningful loss of accuracy.

References

[1] L. L. Vant-Hull, Central tower concentrating solar power (CSP) systems, in: Concentrating solar power technology: principles, developments and applications, Woodhead Publishing - Elsevier, 2012, Ch. 8.
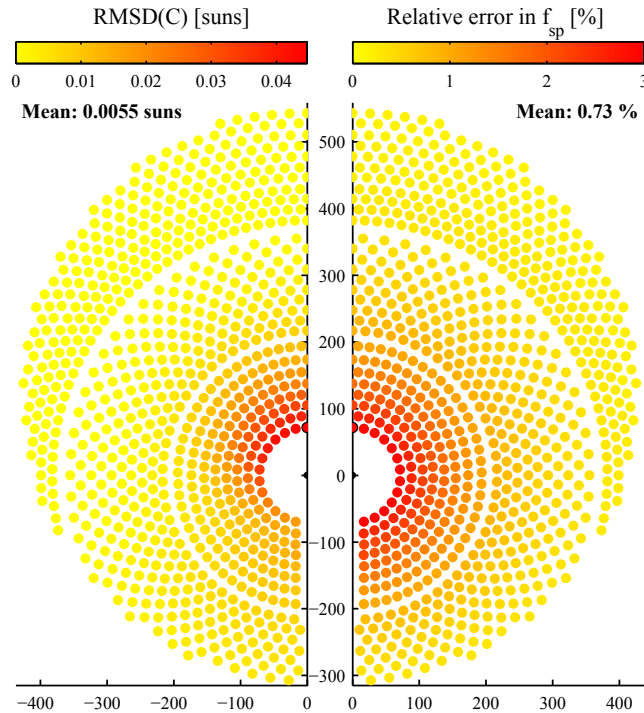URL http://www.sciencedirect.com/science/article/pii/B978184569769350008X

Figure 13: Errors because of flux map shifting respect to direct computation. Root mean square deviation in concentration map (west half) and relative error of spillage loss factor (east half) in Dunhuang field at equinox noon, given $k = 0$ (downwards aiming).

[2] A. Salomé, F. Chhel, G. Flamant, A. Ferrière, F. Thiery, Control of the flux distribution on a solar tower receiver using an optimized aiming point strategy: Application to THEMIS solar tower, Solar Energy 94 (2013) 352–366. doi:10.1016/j.solener.2013.02.025.
URL http://linkinghub.elsevier.com/retrieve/pii/S0038092X1300090X

[3] S. M. Besarati, D. Yogi Goswami, E. K. Stefanakos, Optimal heliostat aiming strategy for uniform distribution of heat flux on the receiver of a solar power tower plant, Energy Conversion and Management 84 (2014) 234–243. doi:10.1016/j.enconman.2014.04.030.
URL http://linkinghub.elsevier.com/retrieve/pii/S0196890414003343

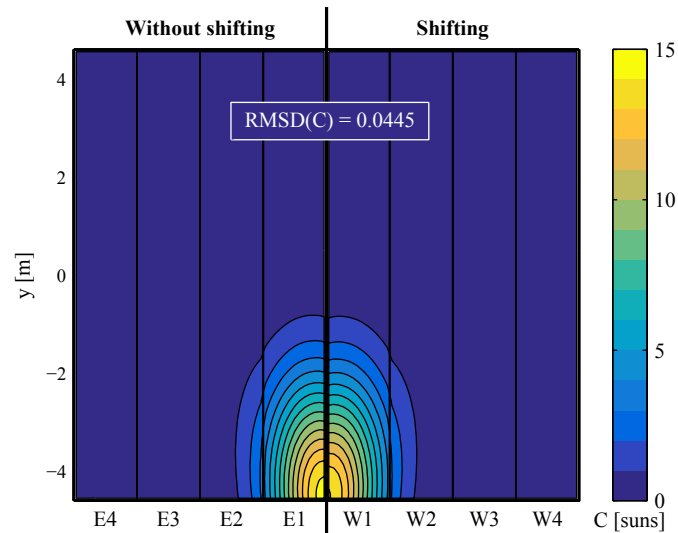[4] Q. Yu, Z. Wang, E. Xu, Analysis and improvement of solar

27

Figure 14: Concentration map at equinox noon for a heliostat (first row, north azimuth), given $k = 0$. Left/East side of the receiver: direct computation. Right/West side of the receiver: mesh shifting.

flux distribution inside a cavity receiver based on multi-focal points of heliostat field, Applied Energy 136 (2014) 417–430. doi:10.1016/j.apenergy.2014.09.008.
URL http://linkinghub.elsevier.com/retrieve/pii/S0306261914009556

[5] K. Wang, Y.-L. He, X.-D. Xue, B.-C. Du, Multi-objective optimization of the aiming strategy for the solar power tower with a cavity receiver by using the non-dominated sorting genetic algorithm, Applied Energy 205 (2017) 399–416. doi:10.1016/j.apenergy.2017.07.096.
URL http://linkinghub.elsevier.com/retrieve/pii/S0306261917309698

[6] B. Belhomme, R. Pitz-Paal, P. Schwarzbözl, Optimization of Heliostat Aim Point Selection for Central Receiver Systems Based on the Ant Colony Optimization Metaheuristic, Journal of Solar Energy Engineering 136 (1) (2013) 011005. doi:10.1115/1.4024738.
URL http://solarenergyengineering.asmedigitalcollection.asme.org/article.aspx?doi=10.1115/1.4024738

[7] R. Flesch, C. Frantz, D. Maldonado Quinto, P. Schwarzbözl, Towards an

optimal aiming for molten salt power towers, Solar Energy 155 (2017) 1273–1281. doi:10.1016/j.solener.2017.07.067.
URL http://dx.doi.org/10.1016/j.solener.2017.07.067

[8] M. Astolfi, M. Binotti, S. Mazzola, L. Zanellato, G. Manzolini, Heliostat aiming point optimization for external tower receiver, Solar Energy 157 (2017) 1114–1129. doi:10.1016/j.solener.2016.03.042.
URL http://linkinghub.elsevier.com/retrieve/pii/S0038092X16002292

[9] N. C. Cruz, J. L. Redondo, J. D. Álvarez, M. Berenguel, P. M. Ortigosa, A parallel TeachingLearning-Based Optimization procedure for automatic heliostat aiming, The Journal of Supercomputingdoi:10.1007/s11227-016-1914-5.
URL http://link.springer.com/10.1007/s11227-016-1914-5

[10] J. García, Y. C. Soo Too, R. Vasquez Padilla, R. Barraza Vicencio, A. Beath, M. Sanjuan, Heat Flux Distribution Over a Solar Central Receiver Using an Aiming Strategy Based on a Conventional Closed Control Loop, in: ASME 2017 11th International Conference on Energy Sustainability, ASME, 2017, p. V001T05A011. doi:10.1115/ES2017-3615.
URL http://proceedings.asmedigitalcollection.asme.org/proceeding.aspx?doi=10.1115/ES2017-3615

[11] T. Ashley, E. Carrizosa, E. Fernández-Cara, Optimisation of aiming strategies in Solar Power Tower plants, Energy 137 (2017) 285–291. doi:10.1016/j.energy.2017.06.163.
URL http://linkinghub.elsevier.com/retrieve/pii/S0360544217311581

[12] L. L. Vant-Hull, M. E. Izygon, C. L. Pitman, Real-time computation and control of solar flux density on a central receiver (Solar Two)(Protection against excess flux density), in: American Solar Energy Society Conference, 1996, pp. 88–94.

[13] F. García-Martín, M. Berenguel, A. Valverde, E. F. Camacho, Heuristic knowledge-based heliostat field control for the optimization of the temperature distribution in a volumetric receiver, Solar Energy 66 (5) (1999) 355–369. doi:10.1016/S0038-092X(99)00024-9.

29

URL   http://linkinghub.elsevier.com/retrieve/pii/
S0038092X99000249

[14] A. Gallego, E. Camacho, On the optimization of flux distribution with flat receivers: A distributed approach, Solar Energy 160 (February 2017) (2018) 117–129. doi:10.1016/j.solener.2017.12.008.

[15] L. L. Vant-Hull, The Role of "Allowable Flux Density" in the Design and Operation of Molten-Salt Solar Central Receivers, Journal of Solar Energy Engineering 124 (2) (2002) 165. doi:10.1115/1.1464124.
URL   http://solarenergyengineering.asmedigitalcollection.
asme.org/article.aspx?articleid=1456457

[16] A. Sánchez-González, D. Santana, Solar flux distribution on central receivers: A projection method from analytic function, Renewable Energy 74 (2015) 576–587. doi:10.1016/j.renene.2014.08.016.
URL   http://linkinghub.elsevier.com/retrieve/pii/
S0960148114004753

[17] A. Sánchez-González, M. R. Rodríguez-Sánchez, D. Santana, Aiming strategy model based on allowable flux densities for molten salt central receivers, Solar Energy 157 (http://dx.doi.org/10.1016/j.solener.2015.12.055) (2017) 1130–1144. doi:10.1016/j.solener.2015.12.055.
URL   http://linkinghub.elsevier.com/retrieve/pii/
S0038092X16001468

[18] M. Rodríguez-Sánchez, A. Sánchez-González, D. Santana, Feasibility study of a new concept of solar external receiver: Variable velocity receiver, Applied Thermal Engineering 128 (2018) 335–344. doi:10.1016/j.applthermaleng.2017.08.173.
URL   http://linkinghub.elsevier.com/retrieve/pii/
S1359431117304143

[19] J. Servert, A. González, J. Gil, D. López, J. F. Funes, A. Jurado, Sensitivity analysis of heliostat aiming strategies and receiver size on annual thermal production of a molten salt external receiver, in: SolarPACES 2016, 2017, p. 030047. doi:10.1063/1.4984390.
URL http://aip.scitation.org/doi/abs/10.1063/1.4984390

30

[20] W. R. Logie, J. D. Pye, J. Coventry, Thermoelastic stress in concentrating solar receiver tubes: A retrospect on stress analysis methodology, and comparison of salt and sodium, Solar Energy 160 (November 2017) (2018) 368–379. `doi:10.1016/j.solener.2017.12.003`.
URL `http://linkinghub.elsevier.com/retrieve/pii/S0038092X17310757`

[21] A. Sánchez-González, C. Caliot, A. Ferriere, D. Santana, Determination of heliostat canting errors via deterministic optimization, Solar Energy 150 (2017) 136–146. `doi:10.1016/j.solener.2017.04.039`.
URL `http://www.sciencedirect.com/science/article/pii/S0038092X17303328`

[22] FluxSPT software tool.
URL `http://ise.uc3m.es/research/solar-energy/fluxspt`

[23] F. Collado, A. Gómez, J. Turégano, An analytic function for the flux density due to sunlight reflected from a heliostat, Solar Energy 37 (3) (1986) 215–234. `doi:10.1016/0038-092X(86)90078-2`.
URL `http://linkinghub.elsevier.com/retrieve/pii/0038092X86900782`

[24] B. Kistler, A user's manual for DELSOL3: Computer code for calculating the optical performance and optimal system design for solar thermal central receiver plants, Tech. rep., Sandia National Laboratories, SAND-86-8018 (1986).

[25] P. Schwarzbözl, M. Schmitz, R. Pitz-paal, Visual HFLCAL - A software tool for layout and optimisation of heliostat fields, in: SolarPACES, Berlin, Germany, 2009.

[26] F. Biggs, C. N. Vittitoe, Helios model for the optical behavior of reflecting solar concentrators, Tech. rep., Sandia National Laboratories, SAND-76-0347 (1979).

[27] M. Schmitz, P. Schwarzbözl, R. Buck, R. Pitz-Paal, Assessment of the potential improvement due to multiple apertures in central receiver systems with secondary concentrators, Solar Energy 80 (1) (2006) 111–120. `doi:10.1016/j.solener.2005.02.012`.
URL `http://www.sciencedirect.com/science/article/pii/S0038092X05000903`